Acid-in-clay electrolyte for wide-temperature-range and long-cycle proton batteries

Shitong Wang[1, 2†], Heng Jiang[3,†], Yanhao Dong[1], David Clarkson[4], He Zhu[5], Charles M. Settens[6], Yang Ren[5,7], Thanh Nguyen[1], Fei Han[1], Weiwei Fan[1], So Yeon Kim[8], Jianan Zhang[9], Weijiang Xue[1], Sean K. Sandstrom[3], Guiyin Xu[1], Emre Tekoglu[1], Mingda Li[1], Sili Deng[9], Qi Liu[5], Steven G. Greenbaum[4], Xiulei Ji[3,*], Tao Gao[2,*], and Ju Li[1,8,10*]

[1]*Department of Nuclear Science and Engineering, Massachusetts Institute of Technology, Cambridge, MA 02139, USA*

[2] *Department of Chemical Engineering, The University of Utah, Salt Lake City, UT 84112, USA*

[3] *Department of Chemistry, Oregon State University, Corvallis, OR 97331, USA*

[4] *Department of Physics and Astronomy, Hunter College, City University of New York, New York, NY 10065, USA*

[5] *Department of Physics, City University of Hong Kong, Kowloon, Hong Kong, 999077, China*

[6] *Materials Research Laboratory, Massachusetts Institute of Technology, Cambridge, MA 02139, USA*

[7] *Advanced Photon Source, Argonne National Laboratory, Argonne, IL 60439, USA*

[8] *Department of Materials Science and Engineering, Massachusetts Institute of Technology, Cambridge, MA 02139, USA*

[9] *Department of Mechanical Engineering, Massachusetts Institute of Technology, Cambridge, MA 02139, USA*

[10] *Lead Contact*

†These authors contributed equally to this work.

*Corresponding authors.

Email: david.ji@oregonstate.edu (X. J.),
taogao@chemeng.utah.edu (T. G.),
liju@mit.edu (J. L.).

SUMMARY

Proton conduction underlies many important electrochemical technologies. We report a series of new proton electrolytes: acid-in-clay electrolyte termed AiCE, prepared by integrating fast proton carriers in a natural phyllosilicate clay network, that can be made into thin-film (tens of microns) fluid-impervious membranes. The chosen example systems (sepiolite-phosphoric acid) rank top among the solid proton conductors in consideration of proton conductivities (15 mS cm^{-1} at 25 °C, 0.023 mS cm^{-1} at −82 °C), the stability window (3.35 V), and reduced chemical activity. A solid-state proton battery was assembled using AiCE as the electrolyte to demonstrate the performance of these electrolytes. Benefitting from the wider electrochemical stability window, reduced corrosivity, and excellent ionic selectivity of AiCE, the two main problems (gasification and cyclability) of proton batteries have been successfully solved. This work also draws the attention of elemental cross-over in proton batteries and illustrates a simple “acid-in-clay” approach to synthesize a series of solid proton electrolytes with a superfast proton permeability, outstanding selectivity, and improved stability for many potential applications associated with protons.

Context & Scale

Proton conductive solid electrolyte is a membrane that allows protons to transfer while blocking other ions and molecules. It is widely used in many essential chemical technologies and processes, like energy storage, energy conversion, electro-synthesis, carbon cycling, and biological applications. However, the existing electrolytes can barely provide high proton conductivity at room and refrigeration temperatures while having expansive electrochemical stability windows and being non-corrosive, low-cost, nonflammable, and nontoxic. Herein, we conceive a new “acid-in-clay electrolyte” (AiCE) approach to prepare a series of novel proton electrolytes. Owing to the advantages of superfast proton permeability, excellent selectivity, and enhanced stability, we demonstrate the superiority of the proton electrolytes in solving two main challenges in proton batteries: gassing and poor cycling performance. More broadly, the AiCE approach opens a new avenue for designing and tailoring electrolyte properties for various electrochemical technologies based on proton conduction.

INTRODUCTION

An electrolyte conducts specific ions between two electrodes in electrochemical devices while forbidding electrons and unintended ions to cross. The electrolyte/separator combination should also have sufficient mechanical hardness to prevent two electrodes from mechanical penetration. Its properties set the boundaries for the performance of electrochemical cells, such as power, energy, and durability[1]. Among various solid electrolytes, the ones that conduct alkali metal ions (especially for Li^+) are extensively developed for rechargeable batteries[2,3]. The developments of lead-acid batteries and hydrogen fuel cells over the past century have witnessed the success of protons in energy storage and conversion[4,5]. Recently, there has been a renewed interest in proton batteries[6-8]; however, the development of high-performance proton batteries is hindered by the gassing problem and the poor cycle life[9]. Due to the narrow electrochemical stability window of bulk liquid water (1.23 V), hydrogen evolution reaction (HER) and oxygen evolution reaction (OER) can be easily triggered in aqueous electrolytes, which restricts the voltage of proton batteries and leads to severe gassing problems[10]. The gassing issues will degrade the volumetric energy density at the battery pack level and cause safety problems. In addition, the acidic electrolytes cause the dissolution of the current collectors or electrode materials[9], resulting in fast capacity degradation. Several strategies have been proposed to address these challenges. One strategy is to broaden the voltage window by coupling an alkaline electrolyte with an acidic one[11,12]. Such design separates the acidic electrolyte from the alkaline electrolyte by multiple cell compartments, adding extra weight and volume to the cell. Alternatively, new proton electrolytes are being investigated. Non-aqueous electrolytes based on aprotic solvents are attractive due to their non-corrosive nature and wide electrochemical stability windows[13,14], but they are limited by the flammability and high cost. Another notable example of the new electrolyte is the water-in-salt electrolytes (WiSE), in which the stability window can be expanded by increasing the molar ratio of salt/water[15]. Yet, the high viscosity and low ionic conductivity remain a problem. Hitherto, none of these strategies has fully addressed the challenges of proton batteries, and few studies examine the elemental cross-over problem, a crucial contributor to capacity fading.

A solid electrolyte is an efficient solution to widen the electrochemical stability window, suppress the dissolution of current collectors/active materials, and prevent side reaction/cross-over of unwanted ions. Nafion™ is the most well-known solid proton electrolyte, but its fast proton conductivity (0.1~100 mS cm^{-1}) can only be maintained at a fully hydrated state (**Table S1**). Polybenzimidazole (PBI), heteropoly acids (HPA), layered hydrates, metal–organic frameworks (MOF), and covalent organic frameworks (COF) are also well developed for solid proton conductors (**Table S1**). However, their proton conductivity is not satisfactory at/below room temperature (10^{-4}~10 mS cm^{-1}, inset in **Figure 2A**). Recently, modified PBI, HPA, and polymers with good proton conductivities have been developed, but most are used in high humidity environments for fuel cells **(Table S1**). Additionally, the narrow electrochemical stability window of water vapor and solution would limit the working voltage of these proton devices.

Natural clays contain abundant hydrophilic groups on the internal surface, which can adsorb proton donors, such as H_2O, acids, or alkalis, by hydrogen bonds or even covalent bonds[16]. The formed composites, also called geopolymers, have been widely used as

binders, adsorbents, pH buffering agents, and catalysts[17-19]. However, few composites have been regarded as solid electrolytes for proton batteries. In this work, we introduce a series of inorganic solid proton electrolytes, denoted as acid-in-clay electrolytes (AiCEs), that will address the gassing, corrosion, and elemental cross-over problems of proton batteries. AiCEs are synthesized by absorbing H_3PO_4 into phyllosilicate clays to form gel-like all-inorganic materials (**Figure 1**). Compared with liquid H_3PO_4 electrolytes, these AiCEs demonstrate superfast proton conductivities (similar as aqueous electrolytes but extended to liquid-nitrogen temperature without phase transition), wider electrochemical stability window (suppressing gassing), enhanced chemical stability (inhibiting corrosion of electrodes/current collectors), and excellent ionic selectivity (restricting unwanted elemental cross-over). As a result, the all-solid proton batteries with AiCEs show excellent proton transport characteristics (33% capacity retention at 720 C under room temperature and 42% capacity retention at 1 C under −60 °C) and cycling performance (20,000 stable cycles at 50 C under room temperature and 3000 stable cycles at 3 C under −20 °C). The AiCE approach not only solves the problems of proton batteries, but also opens a new avenue to design novel proton electrolytes with tunable ionic selectivity, permeability, and stability for other electrochemical applications based on proton conduction.

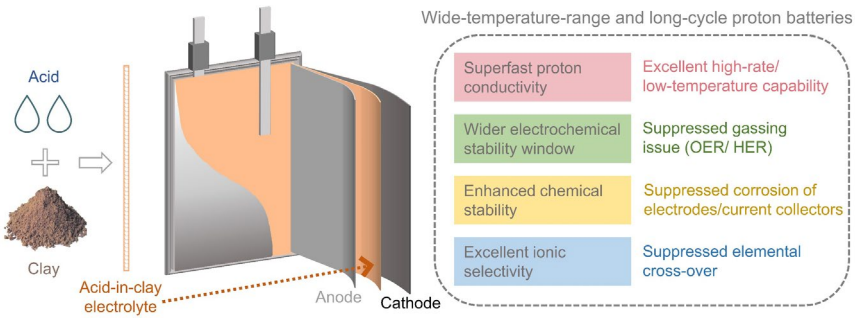

Figure 1. Schematic diagram of acid-in-clay electrolytes and their advantages for wide-temperature-range and long-cycle proton batteries.

RESULTS

AiCE with their kinetics and thermodynamics properties

Based on the ratio of tetrahedra sheets and octahedral sheets in the phyllosilicate network, clay minerals can be classified as 1:1 type (*i.e.*, kaolinite, halloysite), 2:1 type (*i.e.*, montmorillonite, bentonite), and other 2:1 types with rich water channels (*i.e.*, palygorskite, sepiolite)[20]. In this paper, sepiolite is chosen as the first example system for fabricating the AiCE and proton batteries due to its large surface area[21]. After that, the AiCE approach was further demonstrated with another two representative clays, bentonite and halloysite. Thermogravimetric analysis (TGA, **Figure S1**) shows that sepiolite contains 8.7 wt% of adsorbed water and 7.5 wt% of structural water, based on which its chemical formula can be written as $Mg_2H_2(SiO_3)_3{\cdot}3H_2O$. The dry clay powder is barely malleable to make a solid electrolyte. In contrast, the sepiolite becomes a gel-like solid when a certain amount of water (weight ratio of water: clay =1.2:1) is absorbed (**Table S2**) and shows a proton conductivity of σ = 0.096 mS cm^{-1} at 25 °C. Despite the low conductivity, this finding confirms that the absorbed proton donor can enable the clay proton-conductive. Since liquid phosphoric acid has the highest proton conductivity among all known pure

substances[22], the question is whether the proton conductivity of the sepiolite can be further enhanced if phosphoric acid is integrated.

To answer the question, a series of samples were made by mixing phosphoric acid with sepiolite clay powders, in which the proton concentration is tuned by adjusting the molar ratio (*R*) of H_3PO_4/H_2O ranging from 0 to 0.9 (from pure H_2O to 85 wt% H_3PO_4) (**Table S2**). The ionic conductivity of these samples was measured (**Figure S2A**, **Table 1** and **Table S1**), and the maximum values of 15 mS cm^{-1} at 25 °C and 0.023 mS cm^{-1} at −82 °C are obtained when *R*=0.3 (hereinafter denoted as AiCE-S0.3). The activation energy is calculated by fitting the results with the Arrhenius equation. Surprisingly, in the range of 25 °C to −20 °C, it is lower than most of the best proton electrolytes, including fully hydrated Nafion™ (PFSA NR-211) and liquid H_3PO_4, as well as the most conductive solid Li-ion electrolyte (**Table 1** and **Table S4**). In comparison, H_3PO_4 solutions show a maximum conductivity at *R*=0.3 (63 wt% of H_3PO_4, denoted as H_3PO_4-0.3) (**Table S3**, **Figure S2B**). The activation energy of AiCE-S0.3 is slightly lower than that of H_3PO_4-0.3 (**Table 1** and **Table S1**), suggesting the reduced energy barrier for proton conduction in the AiCE. ^1H solid-state nuclear magnetic resonance (NMR) spectroscopy further confirms the fast proton transport in AiCE with an apparent activation energy of 0.15 eV above 0 °C (**Figure S3A-B**). The calculated diffusion coefficients from NMR are 1.4 × 10^{-11} m^2 s^{-1} at 25 °C and 2.1 × 10^{-12} m^2 s^{-1} at −40 °C, respectively (**Figure S3C-D**), comparable to those of liquid H_3PO_4[24]. The excellent proton transport properties could be attributed to the Grotthuss mechanism of the absorbed acid[6,22,25]. Compared with the recently reported solid proton electrolytes[26] and liquid proton electrolytes, AiCE's proton conductivity is among the best (**Figure 2A**, **Figure S4**).

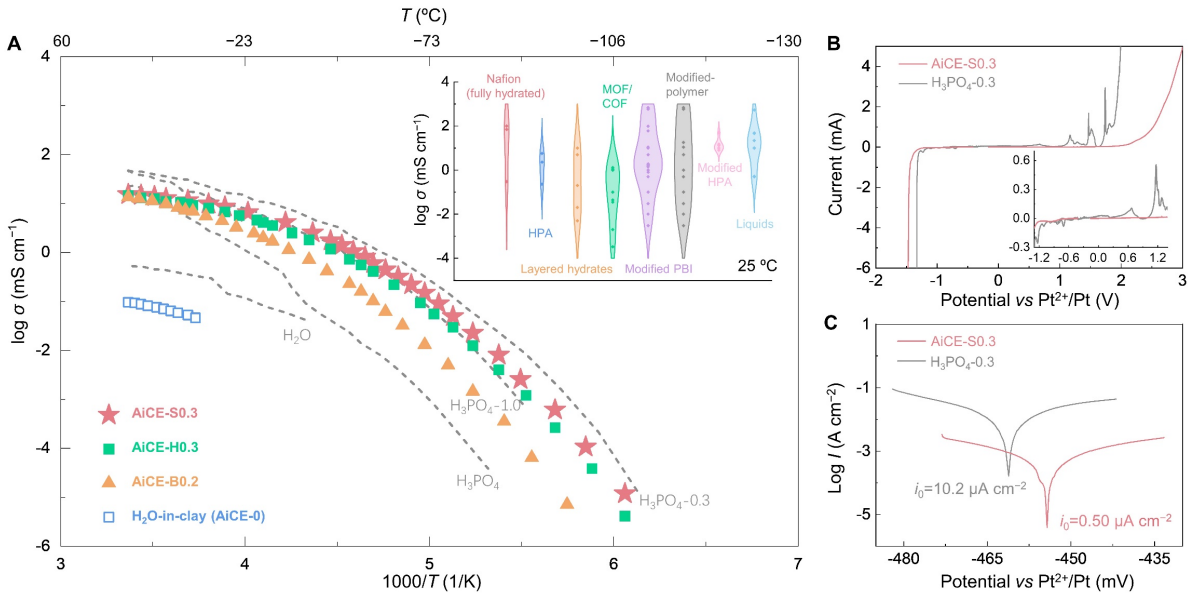

Figure 2. Kinetics and thermodynamics properties of AiCEs

(A) The conductivity comparison of AiCEs (AiCE-S0.3, AiCE-H0.3, and AiCE-B0.2) with liquid electrolytes (H_3PO_4, H_3PO_4-0.3, H_3PO_4-1.0, H_2O), and other solid proton electrolytes (inset). PBI is short for polybenzimidazole; HPA is short for heteropoly acid; MOF is short for the metal–organic framework; COF is short for the covalent organic framework. The references are listed in **Table S1**.

(B and C) Comparison of (B) linear scanning voltammetry at 0.1 mV s^{-1} and (C) Tafel curves about the corrosion on metallic titanium foil of AiCE-S0.3 and H_3PO_4-0.3.

To examine the electrochemical and chemical stability window of the electrolyte, linear scanning voltammetry is first performed (**Figure 2B**). For AiCE-S0.3, HER starts at −1.25 V and OER starts at ~2.1 V (vs Pt^{2+}/Pt), corresponding to an electrochemical stability window of 3.35 V, which is much wider than ~1.6 V of H_3PO_4-0.3. The expanded stability window is beneficial for addressing the gassing problem when high-voltage cathodes and low-voltage anodes are used, which promises enhanced energy density as well as cycling stability. The Tafel plot of Ti electrode is then measured to assess the corrosiveness of the AiCE (**Figure 2C**). The corrosion potential is suppressed from −462 mV for H_3PO_4-0.3 to −454 mV for AiCE-S0.3 (vs Pt^{2+}/Pt). Meanwhile, the corrosion exchange current density is reduced by more than one order of magnitude, from i_0=10.2 μA cm^{-2} to i_0=0.50 μA cm^{-2} for AiCE-S0.3. These results demonstrate the reduced corrosiveness of AiCE-S0.3 toward the Ti current collector.

Table 1. Comparison about proton transport properties of the proton electrolytes in this work

Materials	Activation energy at 25 °C (eV)	Proton conductivity at 25 °C (mS cm^{-1})	Activation energy at −82 °C (eV)	Proton conductivity at −82 °C (mS cm^{-1})
AiCE (sepiolite) (AiCE-S0.3)	0.10	15	0.64	0.023
AiCE (halloysite) (AiCE-H0.3)	0.12	15	0.70	0.013
AiCE (bentonite) (AiCE-B0.2)	0.19	14	0.76	0.001
62 wt% H_3PO_4 (H_3PO_4-0.3)	0.12	46	0.59	0.070
85 wt% H_3PO_4 (H_3PO_4-1.0)	0.25	48	0.74	0.019
100 wt% H_3PO_4 (H_3PO_4)	0.45	22	0.80	2.1×10^{-4}
H_2O	0.12	0.52	0.26 (−42 °C)	0.005 (−42 °C)
Nafion™-211 (fully hydrated)	0.2[26]	0.3	N/A	N/A

Structural study of AiCE

Structural analyses were conducted to study the interactions between the acid and clay. Scanning electron microscope (SEM) images show that the pristine sepiolite comprises fibers of ~100 nm in diameter and several microns in length (**Figure 3A**). The X-ray diffraction pattern shows broad peaks at 10°~30°, suggesting that the sepiolite loses its crystallinity after being mixed with the acid solution (**Figure S5A-B**). The newly formed Si−O−P bonds in Fourier-transform infrared spectroscopy (FTIR) confirm a chemical reaction between acid and clay (**Figure S5C**). The formed gel-like material exhibits Young's modulus of 56 MPa and a hardness of 2.4 MPa, similar to hard rubber, indicating AiCE is a soft solid material (**Figure 3B**). *In situ* cryogenic X-ray diffraction (XRD) results show that no detectable changes in the amorphous structure when the temperature is scanned from room temperature to −83 °C (**Figure 3C**), implying the proton conductive network can be well maintained in a wide temperature range without a drastic phase change, like that of water (water ↔ ice) associated reduction of proton conductivity. The pair distribution function technique is then conducted to investigate the bonding length of local structures **(Figure 3D**). After integrating acid in the clay, the bonding length of the O−H bond in AiCE-S0.3 is obviously shorter compared to that of H_3PO_4-0.3[27], which can explain the enhanced electrochemical/chemical stabilities of AiCE-S0.3.

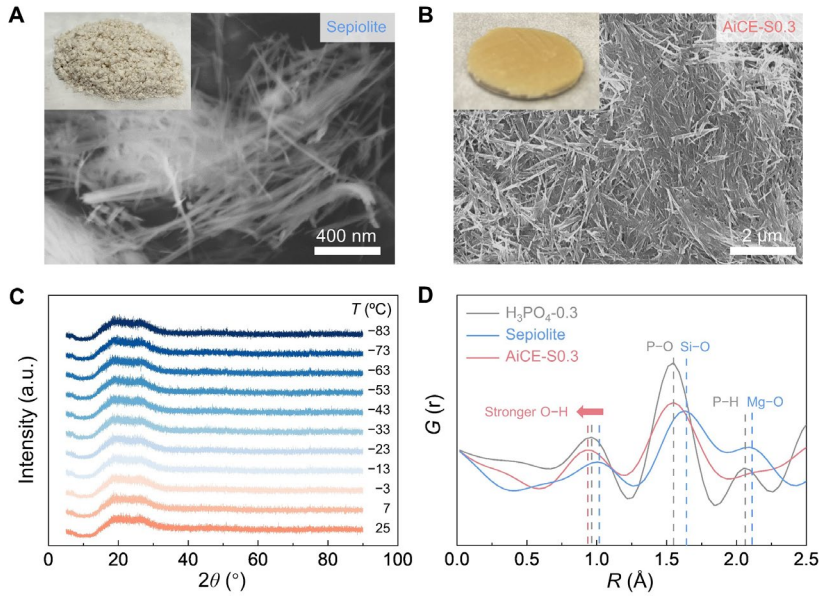

Figure 3. Structural study of AiCE

(A) SEM image of the sepiolite. Inset: image by a camera.
(B) SEM image for AiCE-S0.3. Inset: image by a camera.
(C) *In situ* cryogenic XRD patterns for AiCE-S0.3.
(D) Pair distribution function analysis for H_3PO_4-0.3, sepiolite, and AiCE-S0.3.

Proton batteries with AiCE

The poor cycle life of proton batteries with liquid electrolytes is attributed to several reasons: gassing, dissolution of the current collectors/electrodes by the electrolyte, as well as the subsequent chemical cross-over and contamination of electrodes. Replacing the liquid electrolyte with a non-corrosive and stable solid electrolyte can, in theory, address these problems. However, many all-solid-state batteries suffer poor interfacial contact, poor ionic conductive network in the electrodes, and difficulty in manufacturing due to issues like brittleness and sensitivity to moisture. Here, all-solid proton batteries with AiCE as the solid electrolyte (denoted as SPB) are fabricated in air, using Ti foil, pre-protonated $Cu[Fe(CN)_6]_{0.63}\cdot\square_{0.37}\cdot 3.4H_2O$ (H-TBA) and MoO_3 as the current collector, cathode, and anode, respectively [6,8]. A proton battery with H_3PO_4-0.3 as the liquid electrolyte was made to be the control (denoted as LPB). Compared with the good fluidity of liquid acid, the solid AiCE-S0.3 is difficult to be infiltrated into electrode pores to construct a fast proton conductive network. Therefore, a new recipe of AiCE was developed to enhance its fluidity by increasing the liquid amount by 10% during electrolyte synthesis (**Table S2**), leading to an increased *R* ratio from 0.28 (AiCE-S0.3) to 0.31. For this reason, the new solid electrolyte can be termed AiCE-S0.3'. AiCE-S0.3' shows a similar amorphous structure (**Figure S6A**) as AiCE-S0.3. The Young's modulus (3.6 MPa) and hardness (0.34 MPa) have been successfully decreased by one order of magnitude compared with AiCE-S0.3. As a result, the non-Newtonian fluid property of AiCE-S0.3' (inset in **Figure S6A**) can facilitate its infiltration into the pores of cathode and anode (**Figure S7**). Consequently, the charge transfer resistance of SPB (4.5 Ω) is comparable to that of LPB (5 Ω) [8] (**Figure S8A**). It should be noted that the proton conductivity, electrochemical stability window as well as chemical reactivity of AiCE-S0.3' are quite similar to those of AiCE-S0.3 (**Figure S6B-D**). Although it is crucial for this "non-Newtonian fluid wetting

agent" to improve contact without sacrificing electrochemical/chemical stabilities and proton conductivity, it is hard to use AiCE-S0.3' as the main solid electrolyte owing to its poor film-forming property (tend to cause a short circuit when applying pressure during battery assembling). Therefore, AiCE-S0.3' was used as a "wetting agent" and AiCE-S0.3 was used as a "membrane" in the following SPBs. The thickness of the AiCE-S0.3 membrane is 80 μm and can be made thinner with an optimized synthesis route.

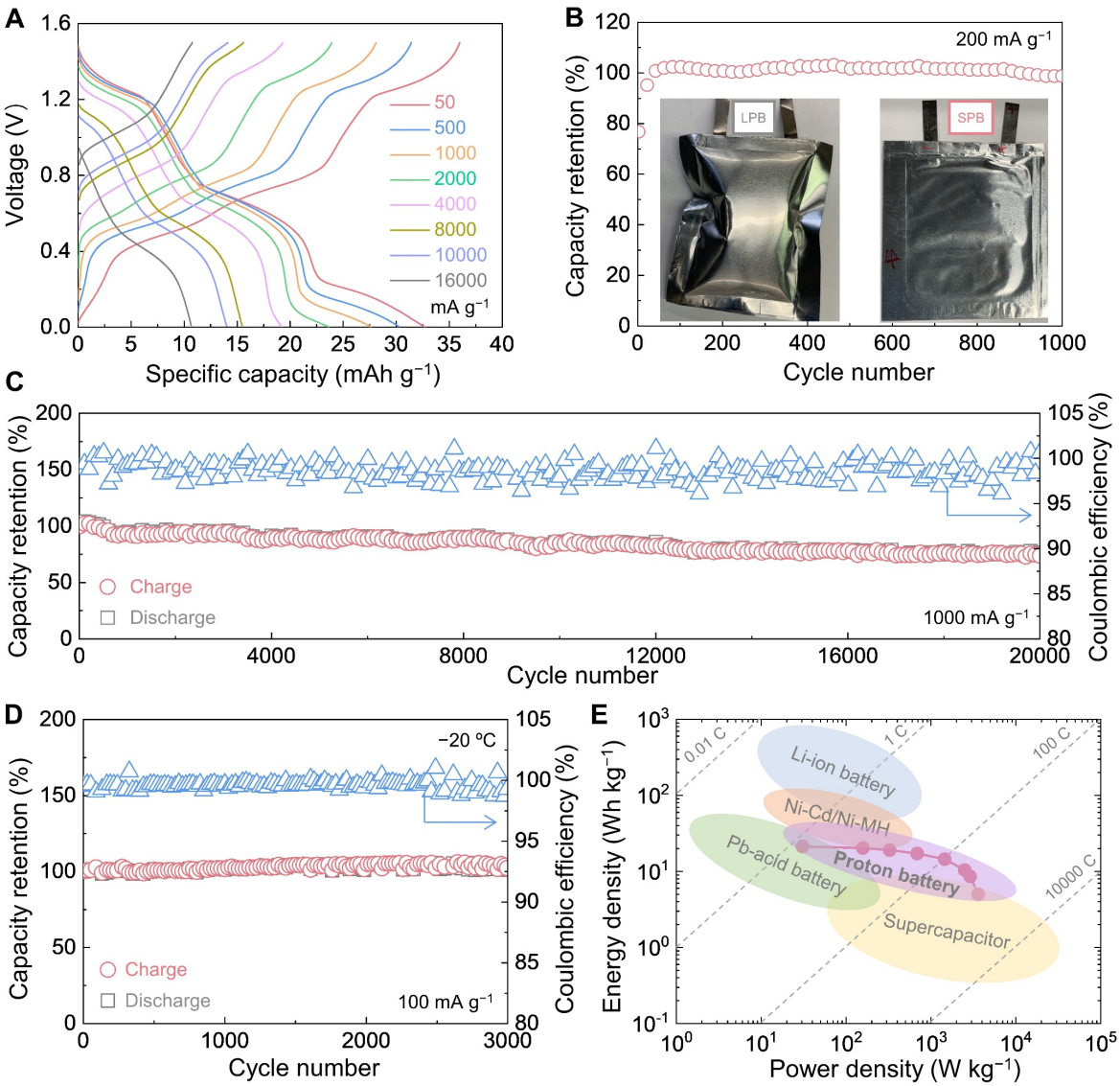

Figure 4. Electrochemical study for proton batteries with AiCE

(A) Galvanostatic charge/discharge potential profiles for SPB at different current rates.
(B) Cycling performance of SPB at 200 mA g^{-1}. Insets are the digital images of pouch cells: LPB after resting for 30 days under 25 °C, and SPB after 1000 cycles under 25 °C.
(C and D) Cyclability and Coulombic efficiency of (C) SPB at 1000 mA g^{-1} under 25 °C, and (D) SPB at 100 mA g^{-1} under −20 °C.
(E) Ragone plot for the proton battery, Li-ion battery, Ni-Cd/Ni-MH battery, Pb-acid battery, and supercapacitor[28,29] (In consideration of energy and power densities for electrodes, the references' values are calculated as double of the real values in cell system, all the specific capacities and energy densities in this work were calculated by using the total mass of cathode and anode, including active materials, conductive carbon and binder).

SPB shows two voltage plateaus at 1.2 and 0.7 V (**Figure 4A** and **Figure S8B**), corresponding to the two redox peaks of MoO_3 (**Figure S9**). It provides a specific capacity of 32 mAh g^{-1} at 50 mA g^{-1} (1.5 C), comparable to lead-acid batteries[28,29], and maintains 33% capacity even at an extremely high current density of 16,000 mA g^{-1} (720 C, **Figure S8C-D**). Such excellent rate performance is comparable to supercapacitors[28,29] (**Figure 4E** and **Table S5**). Low-temperature tests at −60 °C show SPB can keep 42% of the room temperature capacity (**Figure S10A**) and 77% capacity at 500 mA g^{-1} compared to 50 mA g^{-1} at −35 °C (**Figure S10B**). Furthermore, pouch cells of LPB and SPB were assembled to examine the gassing problem at room temperature. Severe gassing was seen in the LPB at the open-circuit voltage (discharged state, **Figure 4B** inset). Current collectors were almost dissolved and purplish liquid leakage was found outside of the pouch cell. These problems prevented further cycling tests of the LPB. In contrast, the SPB pouch cell shows no detectable gassing and stable cycling of 1000 cycles at 200 mA g^{-1} (inset in **Figure 4B** and **Figure S11**). It retains 74% of capacity at the 20,000th cycles when cycled at 1000 mA g^{-1} under room temperature (**Figure 4C**), 100% of capacity at the 3000th cycle when cycled at 100 mA g^{-1} under −20 °C (**Figure 4D**), and 93% of capacity at the 500th cycle when cycled at 50 mA g^{-1} under −35 °C (**Figure S10D**). These results demonstrate that replacing the liquid electrolyte with an AiCE can significantly boost the cycle life of the reported proton batteries (**Table S6**). The energy and power densities of SPB and other energy storage technologies are plotted in **Figure 4E**, where SPB shows better power performance than the lead-acid battery and higher energy density than supercapacitors. To reveal the mechanism behind the improved cycling performance, fundamental studies will be performed and discussed in the next section.

In situ optical microscopy of the batteries shows gas bubbles at both electrode|electrolyte interfaces and current collector|electrolyte interfaces in LPB (**Figure 5A-B**, **Figure S12**, **Video S1~S2**). Particularly, a severe gassing problem happened at the anode side, resulting in the separation of electrode material and current collector. In contrast, no gassing can be seen for SPB even after 480 mins (**Figure 5C**, **Video S3**). The corrosion and dissolution of current collectors and electrodes are quantified by inductively coupled plasma mass spectrometry (ICP-MS) of the cycled liquid electrolyte from the LPB. Mo, Cu, Fe, and Ti elements are present in the cycled liquid electrolyte (**Table S7**), and their amounts correspond to 43.5% dissolution of MoO_3, 35.5% dissolution of H-TBA, and 46.8% dissolution of Ti current collectors (**Figure 5D**). It should be mentioned that the calculated Cu element in the liquid electrolyte is 17.8%, which is 17.7% less than the dissolved amount (molar ratio of Cu: Fe is 1:1 in HTBA). This 17.7% of Cu appears on the anode side due to its cross-over, which is evidenced by the X-ray photoelectron spectroscopy (XPS). Cu signals appear on the MoO_3 in LPB after cycling, demonstrating that the Cu elements at the cathode side can pass through the passivation layer, dissolve into the liquid electrolyte, and cross to the anode side (**Figure S13B**). Besides, Ti signals appear on both cathode and anode of the cycled LPB (**Figure S13A-B**), implying corrosion and dissolution of current collectors by the liquid acid electrolyte. In contrast, no elements from the cathode can be observed on the cycled MoO_3 in SPB, and the absence of Mo, Cu, Fe, and Ti elements in the cycled AiCE-S0.3 further confirms the prevention of cross-over (**Figure S13C**). Based on these results, AiCE is able to prevent gassing, corrosion, and elemental cross-over, therefore enhancing the cyclability of the proton battery.

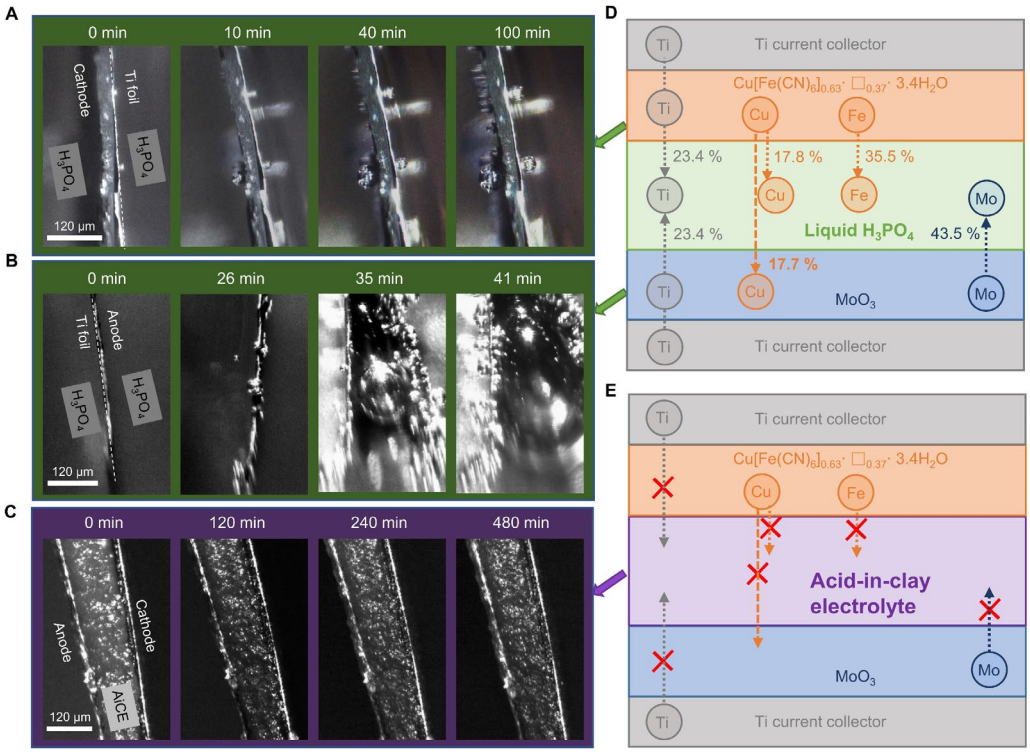

Figure 5. Mechanism study for proton batteries with AiCE

(A-C) *In situ* optical microscopic observation of (A and B) LPB and (C) SPB charged and discharged at 4 C. (D and E) Schematic diagram of the advantages of (E) SPB compared with (D) LPB.

Universality of AiCE approach

Hydrophilic bentonite and halloysite were further investigated to test the AiCE approach. Their formulas are calculated to be $H_2Al_2O_6Si\cdot 1.19H_2O$ (bentonite) and $H_4Al_2O_9Si_2\cdot 0.32H_2O$ (halloysite) based on TGA analysis (**Figure S1**). Similar to sepiolite, dry bentonite and halloysite are barely malleable to make solid electrolytes. After absorbing water, both clays demonstrate proton conductivities (**Figure S14A-B**, more details about the composition ratios are shown in **Table S2**). When H_3PO_4 molecules are absorbed into the structure, a similar gel-like phase with low crystallinity can be obtained (**Figure S14C-D**), which shows enhanced proton conductivity: up to 15 mS cm^{-1} under room temperature, with the optimized composition of R=0.3 for halloysite (AiCE-H0.3), and R=0.2 for bentonite (AiCE-B0.2). The cryogenic proton conductivity and the activation energies of both electrolytes are close to that of AiCE-H0.3 (**Figure 2A** and **Table S4**). The proton conductivity gradually decreases with decreasing temperatures, and 0.013 mS cm^{-1} (AiCE-H0.3) and 0.001 mS cm^{-1} (AiCE-B0.2) can be realized at −82 °C, respectively (**Table 1** and **Table S1**). The outstanding cryogenic proton conductivity of AiCE-H0.3 is consistent with that of AiCE-S0.3, demonstrating the universality of AiCE approach.

DISCUSSION

Based on the discovery and protocol in this work (**Figure 1**), we can see that 1) since there are many more types of natural materials with abundant internal surfaces (like clays, woods[30,31]) than the materials studied in this work, it is reasonable to conjecture that more solid proton electrolytes with superfast proton conductivity and special properties can be

synthesized by integrating proton carriers (water and acids) into the hydrophilic networks. Engineering the chemical properties of these internal surfaces could be a universal approach to modifying their bulk properties and achieving unprecedented performances. 2) The acid-in-clay electrolyte can suppress the chemical reaction kinetics of the protons and structural water, resulting in suppressed gassing problem (HER and OER) and suppressed corrosion of electrodes/current collectors. 3) Fading mechanism by elemental dissolution and cross-over is a long-term issue in redox flow batteries[32] and Li-S batteries[33]. It is also attracting more and more attention in Lithium-ion batteries with manganese spinel[34] and nickel-rich layered cathodes[35,36]. Here, we demonstrate that elemental cross-over could also be an overlooked but important factor for the capacity fading in proton batteries. A solid electrolyte could be an excellent ionic selective membrane to stop elemental dissolution and cross-over for unwanted cations. 4) AiCE is malleable and can be easily made into a fluid-impervious thin membrane, which has the right mechanical properties as a separator. Because its modulus can be easily tuned by the amount of water/acid addition, its non-Newtonian flow behavior in the high water/acid addition limit can be utilized to achieve excellent ionic contact with the active material as well. Besides, AiCE is air/moisture tolerant, enabling the battery to be assembled under ambient conditions. 5) The AiCE approach could also be used in many other applications like electrosynthesis[37], redox flow batteries[32], CO_2 reduction[38], and NH_3 production[39], with the advantages of fast proton conductivity, improved electrochemical window, free-of-crossover and reduced corrosiveness.

EXPERIMENTAL PROCEDURES

Materials synthesis

All the phyllosilicate clays, including sepiolite, hydrophilic bentonite, and halloysite, and phosphoric acid were purchased from Sigma-Aldrich. Nafion™ PFSA NR-211 electrolyte was purchased from FuelCellStore. For a typical synthesis of integrated acid/H_2O in clays, H_3PO_4 acid and H_2O were first mixed to form a uniform solution. Then the above solution was ground with the clay powder in a mortar for several minutes to form a gel. More details about the composition ratios are shown in **Table S2-S3**. Pre-protonated TBA (H-TBA) was synthesized by chemical reduction of $Cu[Fe(CN)_6]_{0.63}\cdot\square_{0.37}\cdot 3.4H_2O$ by N_2H_4 under Ar protection. MoO_3 was prepared by a hydrothermal reaction between $(NH_4)_6Mo_7O_{24}\cdot 4H_2O$ and HNO_3 solution (more details are shown in our previous work)[8]. We further defined the molar ratio (R) of acid/H_2O. The amount of the acid is calculated to 100% H_3PO_4 compound, which is derived from 85 wt% concentrated H_3PO_4 solution; meanwhile, the amount of H_2O is composed of three parts: the H_2O in 85 wt% concentrated H_3PO_4 solution, external added H_2O and H_2O in the phyllosilicate clays (based on the TGA measurement).

Material characterizations

In situ X-ray diffraction (XRD) with a temperature control stage (PANalytical Empyrean Diffractometer; Cu K_α radiation with wavelength λ=1.5418 Å) was used to characterize the phase and the temperature-dependent structural information. Solid electrolytes were assembled in coin cells with a Kapton window that ensures the penetration of an X-Ray beam. The measurements were firstly conducted at 300 K, and then the temperature was set from 300 K to 190 K with a 10 K temperature interval, a ramping rate of 2 K min^{-1}, and

10 min constant temperature rest before each measurement. Pair distribution function measurements were conducted at 11-ID-C beamline at Advanced Photon Source, Argonne National Laboratory. The samples were sealed in capillary tubes. Thermogravimetric analysis (TGA) was carried out using TA Instruments, Discovery with a heating rate of 2 °C min^{-1} in air. The scanning electron microscope (SEM, MERLIN VP Compact) was performed to characterize the morphology. The nanoindentation tests were performed using a TI 950 Triboindenter (Hysitron, Inc.), equipped with a Berkovich diamond tip to examine mechanical properties. The hardness and Young's modulus were evaluated based on the Oliver-Pharr method[40]. Inductively coupled plasma optical emission spectrometry (ICP-OES, Perkin Elmer 2100 DV) was applied to analyze the electrolyte compositions. X-ray photoelectron spectroscopy (XPS) was conducted using PHI Versaprobe II system. Fourier-transform infrared spectroscopy (FTIR) was analyzed on Thermo Scientific™ portable FTIR analyzers. For the ^{1}H solid-state nuclear magnetic resonance spectroscopy (NMR) measurements, the sample was packed into a 5 mm NMR tube under a dry nitrogen atmosphere in a glove bag, sealed with tight-fitting caps and stored in a desiccator. All measurements were performed using a 300MHz (^{1}H frequency) Varian Direct Drive spectrometer and a Doty broadband Z-spec gradient probe.

Electrochemical measurements

To prepare electrodes, active mass, conductive carbon, and binder were mixed with a specific weight ratio of 80:10:10 to form a homogeneous slurry, which was spread on commercial Ti foils (10 μm) and dried at 60 °C in a vacuum for 12 h. The active mass loadings for the MoO_3 anode and H-TBA cathode are around 2.0 mg cm^{-2} (~40 μm) and 4.0 mg cm^{-2} (~15 μm), respectively. The negative: positive capacity ratio was controlled to be ca. 1:1. For the cells with solid electrolytes, a small amount of AiCE-S0.3' was used to wet the electrodes (8 mg cm^{-2}). Then AiCE-S0.3 (~150 μm) was coated uniformly on the surface of the wetted cathode, and the anode was put on the solid electrolyte. Coin cells were assembled by Digital Pressure Controlled Electric Crimper (MTI, corporation), and pouch cells were sealed by an MSK-11A-S vacuum sealer. Some of AiCE-S0.3 was squeezed out of the electrodes by the pressure during cell assembling, resulting in a thickness decrease to ~80 μm. The weight ratio of solid electrolyte: electrodes is 8.1:1. The cells with liquid electrolytes were measured in Swagelok® cells composed of three electrodes and a pouch cell configuration (polyether-sulfone membrane with 100 μm was used as the membrane, the weight ratio of liquid electrolyte: electrodes is 8.0:1), where the detailed procedures were shown in our previous work[8]. All the C-rates in this work are calculated based on the real charge/discharge time. All the specific capacities in this work were calculated using the total mass of cathode and anode, including active materials, conductive carbon, and binder.

Gamry (Reference 3000) electrochemical workstation was used for cyclic voltammetry (CV) and also for electrochemical impedance spectroscopy (EIS) from 0.1 Hz to 1 MHz, with a perturbation of 50 mV applied. To measure the electrochemical stability window, linear scanning voltammetry is also performed by electrochemical workstation in Swagelok® three-electrode cells with Ti rod as the working and counter electrodes, and Pt wire as the reference electrode. *In situ* cryogenic EIS measurements were conducted on a homemade PPMS-Gamry linked platform. Two-electrode devices were first made by using stainless steels as the working and counter electrodes and transferred into the

cavity of PPMS (Quantum Design PPMS® DynaCool™). Then PPMS was used to control the temperatures, and the Gamry electrochemical station was used for EIS measurements. *In situ* optical microscopic measurements were conducted for a homemade cell with an optical micro zoom inspection system (Scienscope, MZ7A). The cell was connected to the Gamry electrochemical workstation for galvanostatic discharge/charge at 4 C at room temperature. For low-temperature measurements, the multi-temperature performance was measured in a biomedical freezer (SANYO) at −20, −35, −50, and −60 °C, where the cells were submerged under isopropyl alcohol solution in a cryogenic storage Dewar mixture. All the cells were tested on a LAND 2001A Cell test system and cycled between 0~1.5 V at different temperatures. For the capacity measurement, ~3 cells were assembled and compared, in which the average one was chosen to demonstrate.

SUPPLEMENTAL INFORMATION

Supplemental Information includes 14 figures, 7 tables and 3 videos and can be found with this article online.

ACKNOWLEDGMENTS

S.W. and H.J. contributed equally to this work. X.J. acknowledges support by National Science Foundation with award No. DMR-2004636. J.L. acknowledges support by NSF DMR-2132647. Q.L. acknowledges the Shenzhen Science and Technology Innovation Commission under grant SGDX2019081623240948. The NMR measurements conducted at Hunter College were supported by grant N00014-20-1-2186 from the U.S. Office of Naval Research.

AUTHOR CONTRIBUTIONS

S.W., H.J., X.J., T.G., and J.L. conceived the project. S.W. synthesized the materials and conducted the characterization. S.W. and H.J. conducted electrochemical testing. Y.R., H.Z and Q.L. contributed to the synchrotron pair distribution function measurements and analysis. D.C. and S.G. contributed to the NMR measurement and analysis. C.S. and W.X. contributed to the *in situ* cryogenic XRD measurements. T.N., F.H. and M.L. contributed to the *in situ* PPMS setup and measurements. W.F. and E.T. contributed to the SEM measurement. S.K. contributed to the nanoindentation measurement and analysis. J.Z. and S.D. contributed to the TGA measurements. S.W., H.J., X.J., T.G. and J.L. wrote the paper. All authors discussed and contributed to the writing.

DECLARATION OF INTERESTS

The authors declare no competing interests.

REFERENCE

1. Li, M., Wang, C., Chen, Z., Xu, K., and Lu, J. (2020). New Concepts in Electrolytes. Chem. Rev. *120*, 6783-6819.
2. Ye, L., and Li, X. (2021). A dynamic stability design strategy for lithium metal solid state batteries. Nature *593*, 218-222.
3. Chen, Y., Wang, Z., Li, X., Yao, X., Wang, C., Li, Y., Xue, W., Yu, D., Kim, S.Y., Yang, F., et al. (2020). Li metal deposition and stripping in a solid-state battery via Coble creep. Nature *578*, 251-255.
4. Jiao, K., Xuan, J., Du, Q., Bao, Z., Xie, B., Wang, B., Zhao, Y., Fan, L., Wang, H., Hou, Z., et al. (2021). Designing the next generation of proton-exchange membrane fuel cells. Nature *595*, 361-369.
5. Winter, M., Barnett, B., and Xu, K. (2018). Before Li Ion Batteries. Chem Rev *118*, 11433-11456.
6. Wu, X.Y., Hong, J.J., Shin, W., Ma, L., Liu, T.C., Bi, X.X., Yuan, Y.F., Qi, Y.T., Surta, T.W., Huang, W.X., et al. (2019). Diffusion-free Grotthuss topochemistry for high-rate and long-life proton batteries. Nat. Energy *4*, 123-130.
7. Zhou, L., Liu, L., Hao, Z., Yan, Z., Yu, X.-F., Chu, P.K., Zhang, K., and Chen, J. (2021). Opportunities and challenges for aqueous metal-proton batteries. Matter *4*, 1252-1273.
8. Jiang, H., Shin, W., Ma, L., Hong, J.J., Wei, Z.X., Liu, Y.S., Zhang, S.Y., Wu, X.Y., Xu, Y.K., Guo, Q.B., et al. (2020). A High-Rate Aqueous Proton Battery Delivering Power Below -78 °C via an Unfrozen Phosphoric Acid. Adv. Energy Mater. *10*, 2000968.
9. Xu, Y.K., Wu, X.Y., and Ji, X.L. (2021). The Renaissance of Proton Batteries. Small Structures *2*, 2000113.
10. Sui, Y., and Ji, X. (2021). Anticatalytic Strategies to Suppress Water Electrolysis in Aqueous Batteries. Chem Rev *121*, 6654-6695.
11. Zhong, C., Liu, B., Ding, J., Liu, X.R., Zhong, Y.W., Li, Y., Sun, C.B., Han, X.P., Deng, Y.D., Zhao, N.Q., and Hu, W.B. (2020). Decoupling electrolytes towards stable and high-energy rechargeable aqueous zinc-manganese dioxide batteries. Nat. Energy *5*, 440-449.
12. Wang, X., Chandrabose, R.S., Jian, Z., Xing, Z., and Ji, X. (2016). A 1.8 V Aqueous Supercapacitor with a Bipolar Assembly of Ion-Exchange Membranes as the Separator. J. Electrochem. Soc. *163*, A1853-A1858.
13. Emanuelsson, R., Sterby, M., Stromme, M., and Sjodin, M. (2017). An All-Organic Proton Battery. J. Am. Chem. Soc. *139*, 4828-4834.
14. Xu, Y., Wu, X., Jiang, H., Tang, L., Koga, K.Y., Fang, C., Lu, J., and Ji, X. (2020). A Non-aqueous H_3PO_4 Electrolyte Enables Stable Cycling of Proton Electrodes. Angew. Chem. Int. Ed. Engl. *59*, 22007-22011.
15. Borodin, O., Self, J., Persson, K.A., Wang, C., and Xu, K. (2020). Uncharted Waters: Super-Concentrated Electrolytes. Joule *4*, 69-100.
16. Kerr, P.F. (1952). Formation and Occurrence of Clay Minerals. Clays Clay Miner. *1*, 19-32.
17. Van Deventer, J.S.J., Provis, J.L., and Duxson, P. (2012). Technical and commercial progress in the adoption of geopolymer cement. Miner. Eng. *29*, 89-104.
18. Duxson, P., Fernández-Jiménez, A., Provis, J.L., Lukey, G.C., Palomo, A., and van Deventer, J.S.J. (2006). Geopolymer technology: the current state of the art. J. Mater. Sci. *42*, 2917-2933.
19. Novais, R.M., Pullar, R.C., and Labrincha, J.A. (2020). Geopolymer foams: An overview of recent advancements. Prog. Mater Sci. *109*, 100621.
20. Murray, H.H. (1999). Applied clay mineralogy today and tomorrow. Clay Minerals *34*, 39-49.
21. Galán, E. (1996). Properties and applications of palygorskite-sepiolite clays. Clay minerals *31*, 443-453.
22. Vilciauskas, L., Tuckerman, M.E., Bester, G., Paddison, S.J., and Kreuer, K.D. (2012). The mechanism of proton conduction in phosphoric acid. Nat. Chem. *4*, 461-466.
23. Teixeira, F.C., de Sá, A.I., Teixeira, A.P.S., and Rangel, C.M. (2019). Nafion phosphonic acid composite membranes for proton exchange membranes fuel cells. Appl. Surf. Sci. *487*, 889-897.
24. Melchior, J.P., Majer, G., and Kreuer, K.D. (2016). Why do proton conducting polybenzimidazole phosphoric acid membranes perform well in high-temperature PEM fuel cells? Phys. Chem. Chem. Phys. *19*, 601-612.
25. Ogawa, T., Aonuma, T., Tamaki, T., Ohashi, H., Ushiyama, H., Yamashita, K., and Yamaguchi, T. (2014). The proton conduction mechanism in a material consisting of packed acids. Chem. Sci. *5*, 4878-4887.
26. Hurd, J.A., Vaidhyanathan, R., Thangadurai, V., Ratcliffe, C.I., Moudrakovski, I.L., and Shimizu, G.K. (2009). Anhydrous proton conduction at 150 degrees C in a crystalline metal-organic framework. Nat. Chem. *1*, 705-710.
27. Tsuchida, E. (2006). Ab InitioMolecular-Dynamics Simulation of Concentrated Phosphoric Acid. J. Phys. Soc. Jpn. *75*, 054801.
28. Aravindan, V., Gnanaraj, J., Lee, Y.S., and Madhavi, S. (2014). Insertion-type electrodes for nonaqueous Li-ion capacitors. Chem. Rev. *114*, 11619-11635.
29. Kabir, M.M., and Demirocak, D.E. (2017). Degradation mechanisms in Li-ion batteries: a state-of-the-art review. Int. J. Energy Res. *41*, 1963-1986.
30. Yang, C., Wu, Q., Xie, W., Zhang, X., Brozena, A., Zheng, J., Garaga, M.N., Ko, B.H., Mao, Y., He, S., et al. (2021). Copper-coordinated cellulose ion conductors for solid-state batteries. Nature *598*, 590-596.
31. Li, T., Chen, C., Brozena, A.H., Zhu, J.Y., Xu, L., Driemeier, C., Dai, J.,

Rojas, O.J., Isogai, A., Wagberg, L., and Hu, L. (2021). Developing fibrillated cellulose as a sustainable technological material. Nature *590*, 47-56.

32. Park, M., Ryu, J., Wang, W., and Cho, J. (2016). Material design and engineering of next-generation flow-battery technologies. Nat. Rev. Mater. *2*, 1.
33. Xue, W.J., Shi, Z., Suo, L.M., Wang, C., Wang, Z.A., Wang, H.Z., So, K.P., Maurano, A., Yu, D.W., Chen, Y.M., et al. (2019). Intercalation-conversion hybrid cathodes enabling Li-S full-cell architectures with jointly superior gravimetric and volumetric energy densities. Nat. Energy *4*, 374-382.
34. Huang, Y., Dong, Y., Li, S., Lee, J., Wang, C., Zhu, Z., Xue, W., Li, Y., and Li, J. (2020). Lithium Manganese Spinel Cathodes for Lithium-Ion Batteries. Adv. Energy Mater. *11*, 2000997.
35. Yoon, M., Dong, Y., Hwang, J., Sung, J., Cha, H., Ahn, K., Huang, Y., Kang, S.J., Li, J., and Cho, J. (2021). Reactive boride infusion stabilizes Ni-rich cathodes for lithium-ion batteries. Nat. Energy *6*, 362-371.
36. Xue, W., Huang, M., Li, Y., Zhu, Y.G., Gao, R., Xiao, X., Zhang, W., Li, S., Xu, G., Yu, Y., et al. (2021). Ultra-high-voltage Ni-rich layered cathodes in practical Li metal batteries enabled by a sulfonamide-based electrolyte. Nat. Energy *6*, 495-505.
37. Shipman, M.A., and Symes, M.D. (2017). Recent progress towards the electrosynthesis of ammonia from sustainable resources. Catal. Today *286*, 57-68.
38. Sánchez, O.G., Birdja, Y.Y., Bulut, M., Vaes, J., Breugelmans, T., and Pant, D. (2019). Recent advances in industrial CO_2 electroreduction. Curr. Opin. Green Sustain. Chem. *16*, 47-56.
39. Qing, G., Ghazfar, R., Jackowski, S.T., Habibzadeh, F., Ashtiani, M.M., Chen, C.P., Smith, M.R., 3rd, and Hamann, T.W. (2020). Recent Advances and Challenges of Electrocatalytic N_2 Reduction to Ammonia. Chem. Rev. *120*, 5437-5516.
40. Oliver, W.C., and Pharr, G.M. (2004). Measurement of hardness and elastic modulus by instrumented indentation: Advances in understanding and refinements to methodology. J. Mater. Res. *19*, 3-20.